

Short Duration Force Measurements in Impulse Facilities

Matthew Robinson* and Klaus Hannemann†

German Aerospace Center (DLR), Bunsenstrasse 10, Göttingen, 37073, GERMANY

A new multiple component stress wave force balance has been designed, calibrated and tested in the High Enthalpy Shock Tunnel Göttingen (HEG) of the German Aerospace Center (DLR). The balance is able to measure forces of short duration (milliseconds) on instrumented models from angles of attack from -40 to 20° . Two models, a blunt cone 303mm long and a standard force reference model (HB-2) of 70mm diameter, are used to establish the accuracy of the force balance. The blunt cone tests were conducted at two different test conditions with a constant Mach number of 7.8 and total enthalpies of 3.0 and 3.5MJ/kg. At 0° angle of attack and an enthalpy of 3.0MJ/kg, the measured axial coefficient was recovered to within 6% when compared to computational fluid dynamic (CFD) simulations. At -10° , the axial and normal coefficients were within 6% and 9% respectively of CFD predictions while the center of pressure (based on chord length) was within 2%. Tests with the HB-2 standard force reference model were conducted at an enthalpy of 12 MJ/kg at an angle of attack of 0° . A linear variation of the axial coefficient with the viscous similarity parameter was predicted with non-equilibrium CFD simulations assuming a laminar boundary layer. The recovered axial force coefficient remained within 5% of the CFD predictions and compared well with experimental results from other wind tunnel facilities. Reasonable comparison of pressure and heat flux measurements along longitudinal symmetry lines of the model was obtained. The accuracy of the force balance is estimated at approximately $\pm 5\%$ for the axial component and $\pm 4\%$ for the normal and pitching moment components.

Nomenclature

\mathbf{g}	Impulse response, -
\mathbf{u}	Input vector, -
\mathbf{y}	Output vector, -
A	Axial force, N
a	Real constant, -
A_s	Reference area, m^2
C	Force coefficient, $\frac{2F}{\rho u^2 A_s}$
C_p	Center of pressure as a percentage of chord, -
F	Force, N
l	Chord length, m
M	Moment, Nm
Ma	Mach number, -
N	Normal force, N
n	Counter, -
P	Pressure, Pa
Q	Heat flux, W/m^2
R	Universal gas constant, 8.3144 J/mol.K

*Research Engineer, Bunsenstrasse 10, Göttingen, 37073, GERMANY, AIAA Member.

†Head of Institute of Aerodynamics and Flow Technology, Bunsenstrasse 10, Göttingen, 37073, GERMANY, AIAA Member.

Re	Reynolds number, -
S	System operator, -
T	Temperature, K
t	Time, s
u	Velocity, m/s

Subscripts

∞	Free-stream
a	Axial direction
d	Diameter, m
i	Integer, -
m	Moment direction
n	Normal direction
t	Total conditions
x	X direction
y	Y direction
z	Z direction

Symbols

χ	Viscous interaction parameter, $Ma_\infty/\sqrt{Re_d}$
η	Angle between velocity vector and element inward normal, radians
γ	Ratio of specific heats, -
ρ	Density, kg/m ³
τ	Shifted time, s

I. Introduction

IN the early era of hypersonics, the high cost and risk of designing complex vehicles precluded experimental prototype flight testing. To overcome this constraint, hypersonic ground based testing facilities were developed and used extensively. Later, as computing resources became more advanced, computational fluid dynamic (CFD) tools were developed. Today however, coupling of the three main methods of hypersonic flight vehicle design, namely hypersonic ground based testing, CFD and flight testing, are becoming economically achievable. Recent projects such as HyShot¹ and SHEFEX² show that hypersonic flight testing of new technologies based on sounding rocket technology can be achieved for an order of magnitude reduction in budgetary requirements compared to complex X-vehicles. This will lead in the near future to more frequent flight tests. However, the requirement of making integrated force and moment measurements in ground-based testing facilities remains a critical and ever increasing aspect in the design process of hypersonic vehicles.

For example, with supersonic combusting ramjets, the shift in the centre of pressure due to combustion is critical. Similarly, real gas effects on re-entry bodies may cause an unpredicted change in the pitching moment, while for missile configurations where target range is of importance, maximization of the lift to drag ratio is critical. For these reasons, a new three-component force balance for the High Enthalpy Shock Tunnel Göttingen (HEG) has been designed, calibrated and tested in order to quantify lift, drag and pitching moment.

Facilities such as the HEG are of great importance since they can produce high Mach number, high pressure test flows which is a critical requirement for scramjet research and also high enthalpy flows with the correct binary scaling requirements for re-entry flow studies. However, for such facilities, the test time is limited in duration to the order of milliseconds and for a force balance to operate on these short time scales, it becomes necessary to have a very short response time. Unfortunately, conventional force measurement techniques do not possess the required response times, thus making force measurement in impulse facilities a non-trivial matter. However, progress has been made in recent years to develop techniques which enable successful measurement of forces over short time scales.

These techniques include using very light models with stiff balances including the application of vibration compensation methods via the use of accelerometers. Other techniques include using free-flying or weakly constrained models and measuring the corresponding accelerations to infer the applied aerodynamic forces.

However, in this paper, a different technique that relies on the ability to measure the dynamic response of the model and support structure through the propagation of stress waves is utilized. In order to quantify

the accuracy of the balance, two models mounted on the force balance have been tested in the HEG, the results of which are presented in this paper. The first model, a blunt cone of length 303mm, was tested at angles of attack from 0 to -20° at low enthalpies (3-4MJ/kg). The second model, HB-2, is a standard force reference model and was tested at an enthalpy of 12MJ/kg.

II. Force Measurement Technique

1. Introduction

Advances have been made in the last two decades on techniques for measuring forces in flows with very short durations, such as occur in impulse hypersonic facilities (e.g.³⁻⁵). These techniques vary from measuring model accelerations, model and support strains including acceleration compensation to visualization methods utilizing free-flying models.

One other technique, which has proved suitable for force measurement in impulse facilities, is the stress-wave force-balance technique (SWFBT), originally proposed for single-component (drag) force measurement.⁶ This technique has been extended for measurement of the three components of force on a cone at incidence⁷ and has been used to measure the thrust produced by scramjet vehicles, with fuel injection and combustion, for models with symmetry about the thrust axis.^{8,9} The SWFBT relies on the ability to measure the dynamic response of the model and supporting structure and consequently any effects such as model flexibility and mass distribution are accounted for.

2. Force Recovery Technique

The stress wave force measurement technique involves measuring stress waves which propagate and reflect through the model and support structure. Upon flow arrival, stress waves propagate through the model at the speed of sound of the material and subsequently enter a stress bar which is instrumented with a strain gauge to record the time history of strain. If the model and support structure produce linear strains due to linear forces, then the dynamic behavior of the system can be modeled as time-invariant, casual, and linear with an output $\mathbf{y}(t)$ (the resulting strain signal), being related to the applied aerodynamic load, $\mathbf{u}(t)$, via an impulse response function, $\mathbf{g}(t)$, as described by the convolution integral,

$$\mathbf{y}(t) = \int_0^t \mathbf{g}(t - \tau)\mathbf{u}(\tau)d\tau. \quad (1)$$

The assumptions of a time-invariant, casual, and linear system require that,

- * $S(u_1(t) + u_2(t)) = S(u_1(t)) + S(u_2(t))$,
- * $S(a * u_1(t)) = a * S(u_1(t))$,
- * $y(t - \tau) = S(u(t - \tau))$ if $y(t) = S(u(t))$, and
- * $y(t)$ at any time t depends only on $u(t)$ for times less than t ,

where S is the system operator and a is a real constant.

Since the data recorded are discretized (i.e. $\mathbf{u}(t)$, $\mathbf{y}(t)$ and $\mathbf{g}(t)$ can be replaced by u_i , y_i and g_i with $i = 0, 1, 2, 3 \dots n$), Eq. 1 can be written as shown in Eq. 2 with a sampling rate of Δt ,

$$y_i = \sum_{j=0}^i g_{i-j}u_j\Delta t. \quad (2)$$

The aerodynamic force in an experiment can be determined by the deconvolution of the strain signal with the impulse response function. The impulse response function is determined either through experiment or through finite element analysis (FEA), however in order to reduce errors due to modeling approximations it is usually preferable to determine the impulse response experimentally as was done for these experiments.

A number of iterative deconvolution schemes exist for the solution of Eq. 1. The algorithm proposed by Prost and Goutte¹⁰ was used exclusively in this paper. This algorithm solves the discrete convolution equation using functional minimization with the extended conjugate gradient algorithm.

Consider a three component system with input vectors \mathbf{u}_N , \mathbf{u}_A and \mathbf{u}_M and output vectors, \mathbf{y}_N , \mathbf{y}_A and \mathbf{y}_M , where the subscripts N , A and M represent the normal, axial and pitching moment components respectively. If the signals are discretized at time step Δt , the three output vectors can be related to the three input vectors by,

$$\begin{pmatrix} \mathbf{y}_N \\ \mathbf{y}_A \\ \mathbf{y}_M \end{pmatrix} = \begin{bmatrix} \mathbf{g}_{NN} & \mathbf{g}_{NA} & \mathbf{g}_{NM} \\ \mathbf{g}_{AN} & \mathbf{g}_{AA} & \mathbf{g}_{AM} \\ \mathbf{g}_{MN} & \mathbf{g}_{MA} & \mathbf{g}_{MM} \end{bmatrix} \begin{pmatrix} \mathbf{u}_N \\ \mathbf{u}_A \\ \mathbf{u}_M \end{pmatrix} \Delta t. \quad (3)$$

Here, there are nine square sub-matrices relating each of the outputs to each of the inputs. Again, the impulse responses are found either experimentally or using FEA. Multiple-component deconvolution is used to determine the three components of aerodynamic load from the three measured output signals.

A program named “DECON”, written in the C programming language solves Eq. 3 for n components. The program also includes several other tools such as file manipulation, data averaging and statistics. Also included is a Newtonian solver for force/moment prediction which is further described in section V.

Several additional steps can be performed to increase the accuracy of the recovered forces, especially in performing multiple component deconvolution. Firstly, since the deconvolution scheme is iterative in nature, the deconvolution can be started from an initial solution. It has been found that using a starting solution based on either a Newtonian or a CFD prediction of the forces and moments, scaled with the time history of Pitot pressure, offers the best accuracy.

Further, conditioning the impulse and output signals to account for differences in force magnitudes between the different components also increases the accuracy of the recovered signals. An additional measure to optimize the combination of strain measurements to reduce the cross-coupling between components has also been implemented in “DECON”.

III. Models

A. Blunt Cone

The 8kg steel test model (see Fig’s. 1 and 2) consisted of a blunt 10.0° half angle cone. The model, 303.0mm in length, had a tip radius of 7.8mm and a base diameter of 120.0mm. The model also contained two longitudinal lines of three calibration positions in the axial-normal plane. Each calibration point spanned 90.0mm sequentially starting from the cone tip with an additional calibration position located on the center axis at the tip. This provided a total of seven calibration positions.

Small rectangular shaped steel lugs of 24.0mm in length and 10.0mm in width were used to provide a flat surface on which an instrumented impact hammer (PCB model 086C04) was used to apply a known force in the axial and normal directions on the curved surfaces of the cone. The effect of the lugs on the dynamic response of the system was small as their mass was approximately 0.1% of the total model mass.

The conical model also contained a taper cavity 109.0mm in depth in which the balance was mounted. A locking plate, containing an array of 12 M6 cap screws, was used to mount the balance taper into the model cavity, thus ensuring a tight press fit. Four additional M6 screws were inserted through the front of the balance for additional closure (not shown in Fig. 1).

Two side pressure transducer mounts were located in the conical model 270.0mm from the cone tip and separated circumferentially either side from the axial-normal plane by 79° (the locking plate bolt holes prevented the sensors from being located 180° apart).

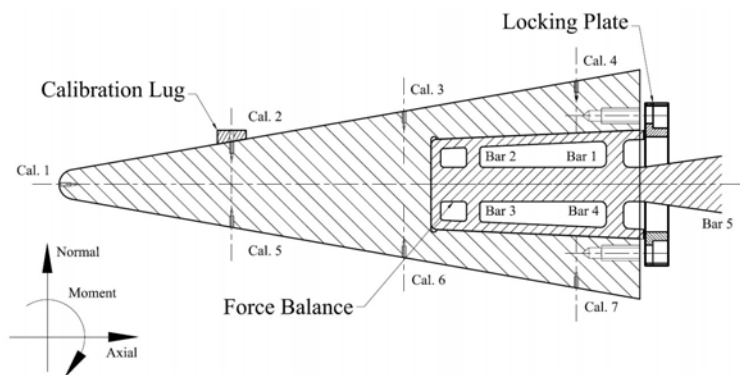


Figure 1. Conical model.

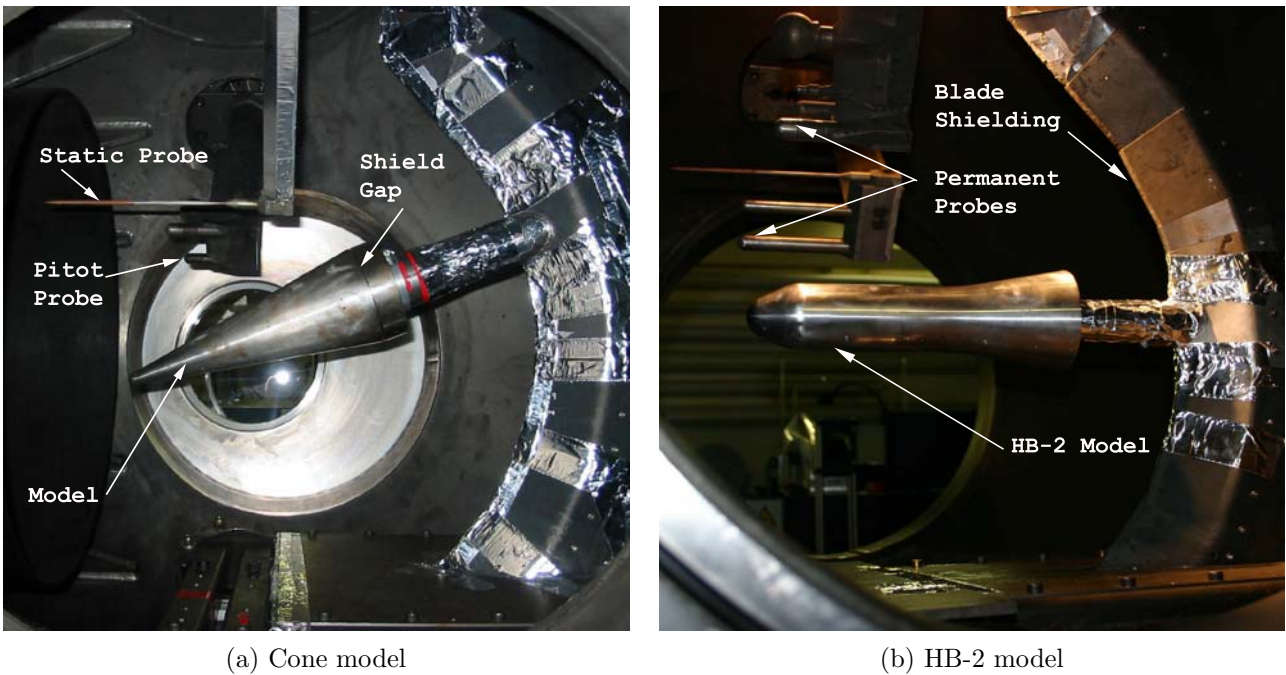


Figure 2. Cone and HB-2 models installed in the HEG test section.

B. Hypersonic Ballistic Model 2

The Hypersonic Ballistic Model 2, HB-2, is a standard force reference model.^{11,12} A diameter, d , of 70mm was chosen such that the model fitted onto the force balance and similar ranges of the viscous similarity parameter could be obtained as in the open literature.

The steel model, 343.0mm in length, contained 12 pressure transducers and 17 heat transfer mountings. However, in the experiments only 16 of the 17 heat transfer tappings were utilized due to space restrictions. The model consists of a spherical nose of 21mm radius, a cylindrical body and a trailing 10° flare. Two sectional views detailing slices through the pressure and heat transfer gauges are shown in Fig. 3 (a) while a photograph of the disassembled model is shown in Fig. 3 (c). The force balance was mounted within the conical taper seen in Fig. 3 (c) and held in place by four M6 socket head cap screws.

The force balance sting was shielded by a 129mm long cylindrical steel tube of 44mm in diameter. This shielding differs slightly from the nominal design provided in Gray¹¹, however the larger shielding is expected to have a negligible impact on the force coefficients due to the low pressure in the wake region.

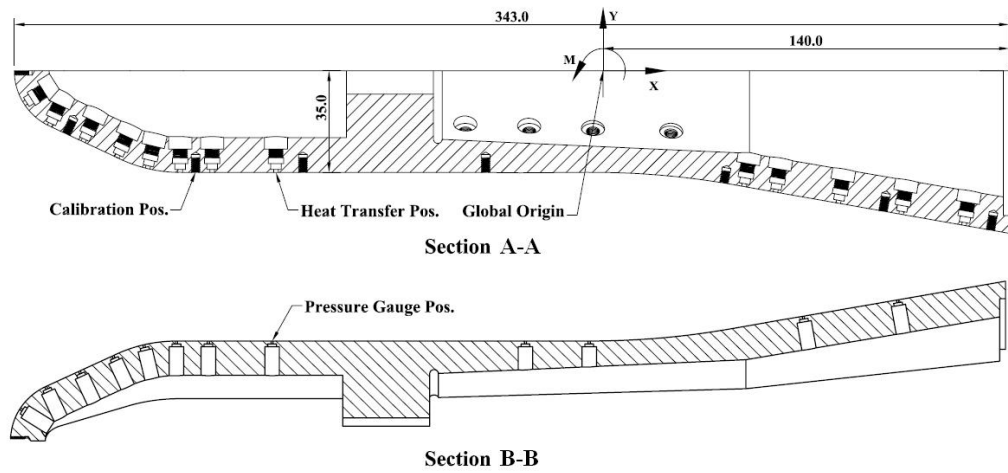
C. Instrumentation

The conical model was instrumented with two XCS-093 Kulite semiconductor pressure transducers. Further to this, a total of five additional XCS-093 Kulite semiconductor pressure transducers was used to measure the build up of back pressure within the force balance shielding (see Fig. 2 (a)).

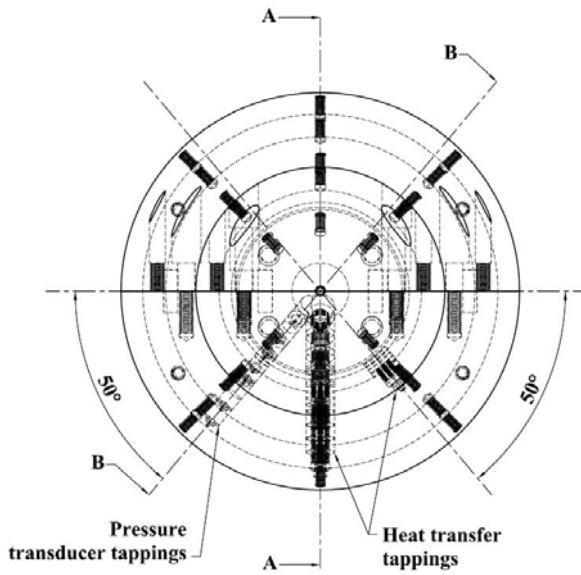
The HB-2 model contained 12 XCS-093 Kulite semiconductor pressure transducers. One additional transducer was used to measure the pressure on the trailing back surface. A total of 15 heat transfer gauges (Medtherm Type E) was installed in the model.

Strain gauges were applied to each stress bar. Strain was measured simultaneously using UCP120 Kulite semiconductor gauges mounted on the normal stress bars while ACP120 gauges were used to measure the strain in the axial stress bar. Each gauge was connected in a half Wheatstone bridge arrangement. The signals were amplified using an in-house amplifier.

All data during a run were sampled at $1.0\mu\text{s}$ for 51.2ms after triggering. Prior to triggering, the data were sampled at $10.0\mu\text{s}$ for 1020.0ms. Strain calibration data were sampled at $10.0\mu\text{s}$ for 200.0ms. Post processing of run strain data were performed at a sampling rate of $10.0\mu\text{s}$.



(a) HB-2 sectional views. Dimensions in millimeters.



(b) Schematic side view of HB-2.



(c) Disassembled HB-2 wind tunnel model.

Figure 3. HB-2 wind tunnel model.

IV. Test Facility

The High Enthalpy Shock Tunnel Göttingen (HEG) is a free-piston driven shock tunnel of approximately 62m in length. It produces a test time of milliseconds in duration at stagnation pressures of up to 200MPa and stagnation enthalpies of up to 24MJ/kg.¹³ For the current series of experiments, runs at conditions III (HB-2 model, medium enthalpy), and conditions XI and XII (cone model, low enthalpies) were performed. The low enthalpy tests were performed using a carbon fiber contoured Mach 8 nozzle while the medium enthalpy tests were performed using a conical Mach 8 steel nozzle. The nominal test conditions are summarized in Table 1.

Table 1. HEG nominal test conditions.

Condition	P_∞ Pa	T_∞ K	ρ_∞ kg/m ³	H MJ/kg
III	790	800	0.0033	12
XI	1650	230	0.0246	3
XII	745	260	0.0098	4

A one dimensional code, ESTC¹⁴, was used to determine the nozzle supply temperature and enthalpy of the flow. For the high enthalpy conditions, the free-stream conditions were determined using the numerical re-building approach as described in Hannemann.¹³ For the low enthalpy tests, the free-stream temperature was calculated using the total enthalpy and Mach number^a. The free-stream density was calculated via the Rayleigh Pitot formula and the measured Pitot pressure. Lastly, the free-stream pressure was calculated using the ideal gas law with the ratio of specific heats (γ) set to 1.4.

In HEG, an indication of the time it takes for the nozzle flow to establish can be obtained by normalizing the Pitot and static pressures by the nozzle supply pressure, with an appropriate time delay to account for the time it takes the flow to pass from the nozzle supply region to the probes. The end of the test time is usually dictated by contamination. In general, usable test times of 0.5 and 4.0ms were obtained for condition III, and conditions XI and XII respectively (see Fig. 4).

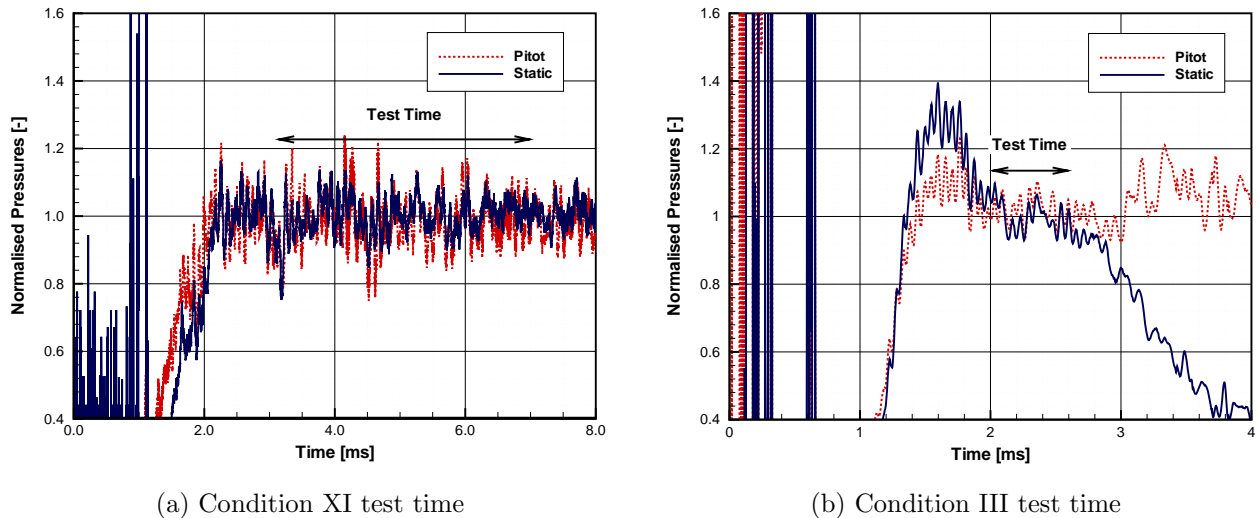


Figure 4. Useable test times for conditions III and XI.

^aThe Mach number was determined by simulating the nozzle flow with the DLR CEVCATS-N CFD code^{13, 15} with the assumption of thermal non-equilibrium flow. The nozzle boundary layer was modeled as fully turbulent using the Baldwin Lomax algebraic model.

V. Force Prediction

The prediction of forces and moments on a wind tunnel model is an important and sometimes critical exercise. This is especially important for test campaigns involving the measurement of forces but is also of importance in more general test campaigns (e.g. determining whether the structural integrity of the model and support structure is adequate to withstand the aerodynamic loading from the test). Consequently, for this paper, detailed force and moment predictions using two methods were performed. For the initial model and balance design, a simple Newtonian prediction was made but for comparison of the experimentally measured forces and moments, CFD simulations were performed. Details for each method are briefly described.

A. Newtonian

A Newtonian force prediction code was written in the C programming language. The Newtonian method provides a simple yet extremely fast and relatively accurate prediction (for blunt bodies) of the applied forces and moments. The code is included as a force prediction module in the “DECON” suite. The code takes P_∞ , $u_{x\infty}$, $u_{y\infty}$, $u_{z\infty}$, R , γ and ρ_∞ as inputs as well as a description of the geometry. The geometric description consists of a node file containing x , y and z co-ordinates and an element file detailing nodal connectivity information. The node and element files can be created using an external meshing program (e.g. the ANSYS FEA program was used in this paper) or by analytical methods to define the geometry.

Computation of the surface pressure is determined using Eq’s. 4 and 5, where p is the impact pressure, P_{o2} is the stagnation pressure behind the normal shock and η is the angle between the velocity vector and the surface element inward normal vector.

$$\frac{p}{P_\infty} = 1 + \left(\frac{P_{o2}}{P_\infty} - 1 \right) \cos^2 \eta, \text{ and} \quad (4)$$

$$\frac{P_{o2}}{P_\infty} = \left[\frac{(\gamma + 1)^2 Ma_\infty^2}{4\gamma Ma_\infty^2 - 2(\gamma - 1)} \right]^{\frac{\gamma}{\gamma - 1}} \frac{1 - \gamma + 2\gamma Ma_\infty^2}{(\gamma + 1)}, \quad (5)$$

The code also has the option of either performing a Prandtl Meyer expansion for shadow regions or setting the shadow regions equal to the free-stream pressure.

In the case of a Prandtl Meyer expansion, the expansion angle is taken as the angle between the element and the free-stream velocity vector. Thus, the implementation of this feature has been somewhat simplified since no information regarding the upstream flow properties from the adjacent element(s) is used. For blunt body configurations, the determination of the pressure acting on the shadow regions is largely negligible for the total force prediction.

An example mesh for the HB-2 model and the corresponding computed pressures is illustrated in Fig. 5. For this simulation, the model was inclined at 30° angle of attack and simulated at HEG condition XI. The computational time for this simulation on a windows based Intel Pentium 1.6GHz with 512MB RAM was less than one second.

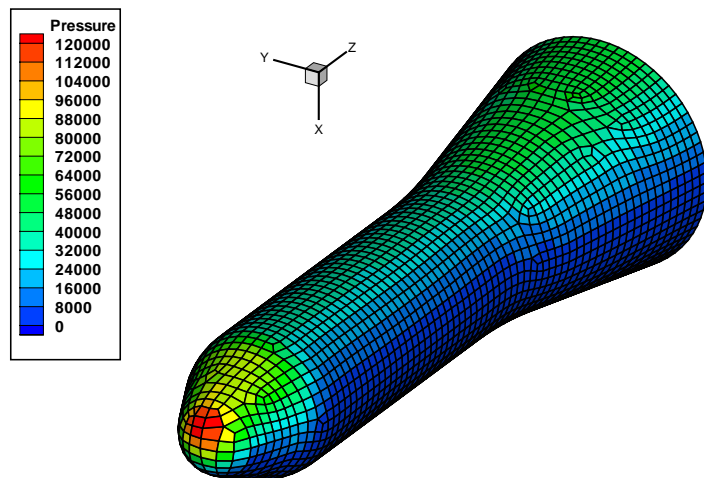


Figure 5. Newtonian mesh of HB-2 model with contours of pressure (in Pa). Shadow regions computed with a Prandtl Meyer expansion.

B. CFD

For more accurate predictions of forces and moments, the DLR-TAU CFD code was utilized.¹⁶ This code uses an unstructured hybrid three-dimensional adaptive finite volume multi-grid method to solve the Reynolds-averaged Navier-Stokes equations and is optimized for both vector and parallel computers.

1. CFD Prediction for the Cone Model

Computations were performed with a perfect gas assumption. In order to simulate angles of attack, a structured three-dimensional grid was used. The mesh was composed of 90 cells in the body normal and conical body directions and 50 cells circumferentially. Symmetry was exploited along the axial-normal plane of the cone. Cells were clustered towards the model to ensure adequate resolution of the boundary layer such that the maximum surface y -plus value was less than unity.

An isothermal boundary condition with both turbulent and laminar boundary layer assumptions was simulated^b.

Nominal angles of attack of 0, -10 and -20° at the calculated run conditions were simulated using the AUSMDV second order upwind scheme (see Fig. 6). Comparisons of the side pressures showed that the measured values on the conical model were generally within 5% of the CFD values indicating that the free-stream conditions and modeling assumptions were sufficiently accurate to obtain reasonable estimates of the forces as most of the force is due to pressure loads.

2. CFD Prediction for the HB-2 Model

Simulations were performed using an axisymmetric structured mesh composed of two blocks. The first block, comprising of the model windward surface, had 101 by 291 points while the second block, simulating the wake region, had 61 by 31 points. A grid refinement study showed this mesh had suitable resolution over all of the conditions simulated.

A laminar boundary layer on isothermal walls of temperature 300K was assumed for all surfaces except for the sting shielding which was simulated as an Euler wall. The 11 species air reaction model of Gupta *et al.*¹⁷ was assumed for the non-equilibrium simulations. The AUSMDV 2nd order solver was utilized with a least squares gradient reconstruction. No account for the conical nozzle flow was made to the far-field boundary condition, hence it is expected that the pressure will be slightly over-predicted along the model.

Shown in Fig. 7 is the HB-2 CFD mesh along with contours of Mach number at condition III. Profiles of measured pressure and heat flux are compared to CFD in Fig. 13.

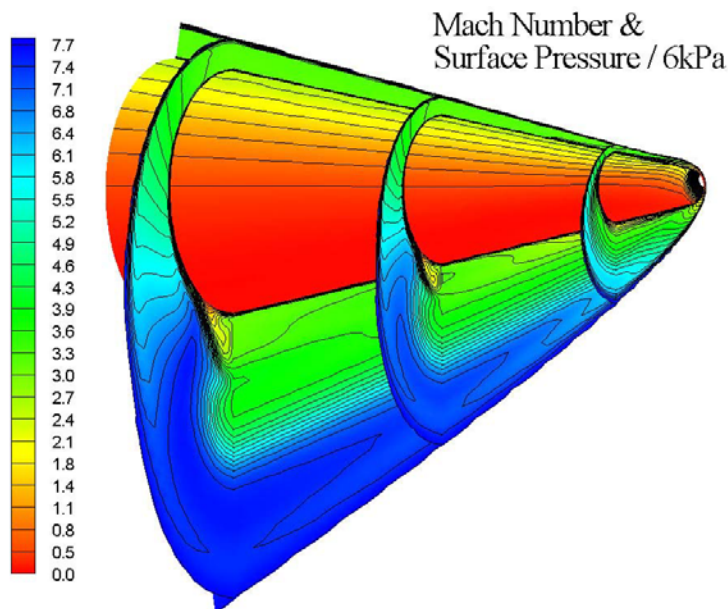


Figure 6. CFD Mach number and surface pressure contours for the cone model at -10°.

^bFor condition XI, the Reynolds number based on chord length was approximately 1.1×10^6 while for condition XII it was approximately 0.5×10^6 . The Spalart Allmaras model with Edward's modification was used to model the turbulent boundary layer flow.

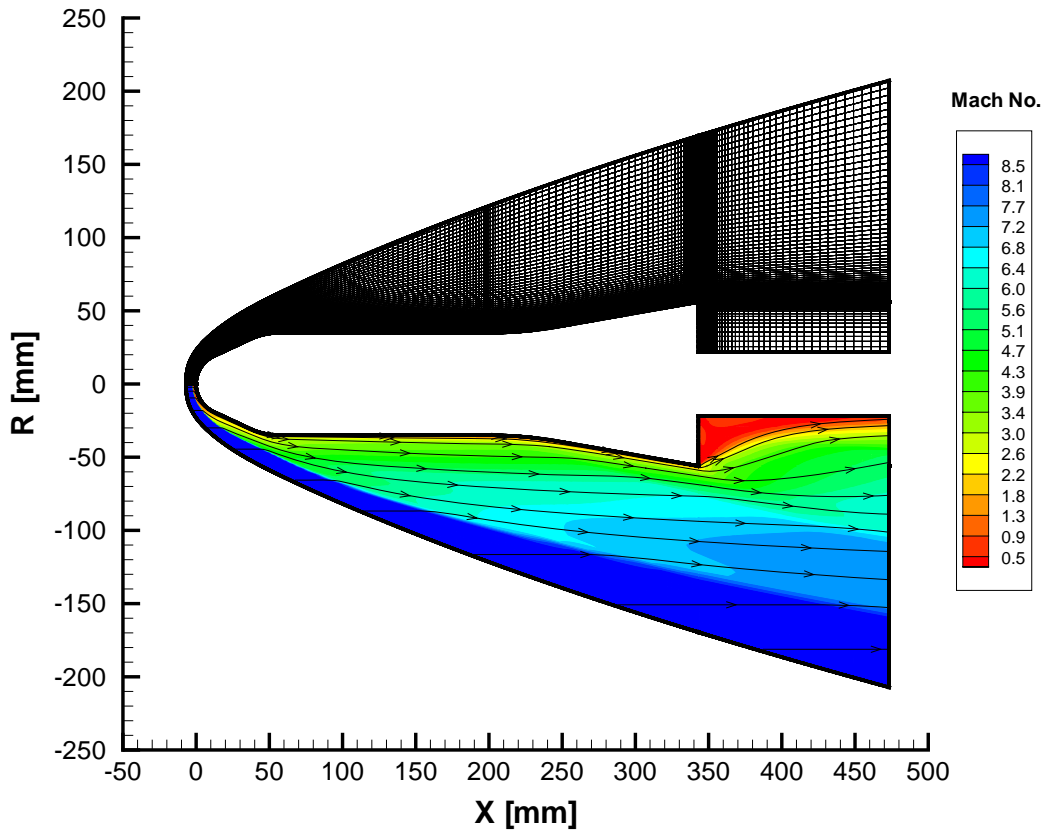


Figure 7. CFD mesh and contours of Mach number for the HB-2 model.

VI. Experimental Results

A. Blunt Cone Model

1. Condition XI

The recovered time histories of force are shown in Fig. 8 (a) for run 687. It is noted that the corrected^c axial force (i.e. the drag force at zero angle of attack) is steady over the test time.

The resolution of the balance can also be gauged by noting the recovered drag force successfully captures the oscillations (hypothesized to be due to compression and expansion waves which reflect between the piston and the end of the compression tube) as reflected in the measured Pitot pressure.

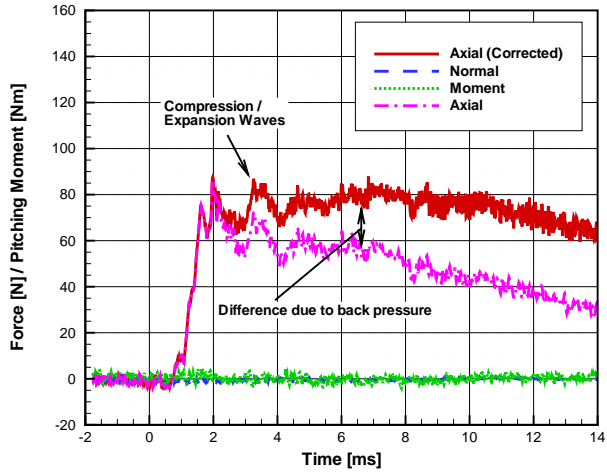
Normalization of the measured forces to force coefficients is shown in Fig. 8 (b) along with the theoretical estimates from the CFD. It is noted that the recovered time histories compare well with the values from the CFD solutions. In general, relative errors of 6%, 1% and 1% are obtained between the recovered axial, normal and moment coefficients respectively to the CFD values.

2. Condition XII

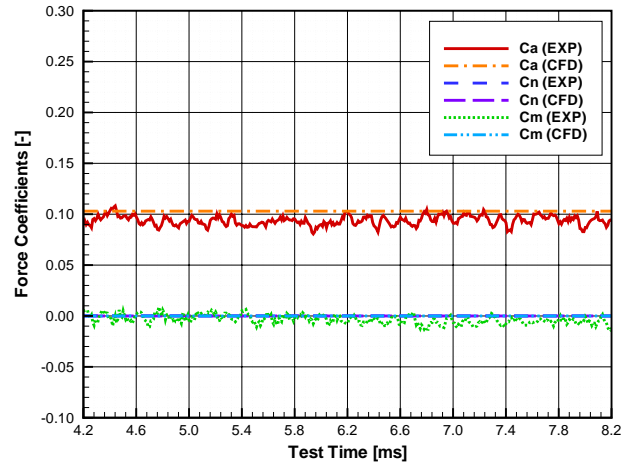
The majority of runs was conducted at condition XII with a variation in angle of attack. Nominal angles of attack of 0, -10 and -20° were tested.

Figure 9 (a) gives an example of the recovered time histories of force from run 685. Also shown is the time history of Pitot pressure. It is seen that the force time histories closely follow the time history of Pitot pressure.

^cThe “corrected” axial force is obtained through the multiplication of surface area and the measured back pressure plus the deconvolved thrust force.

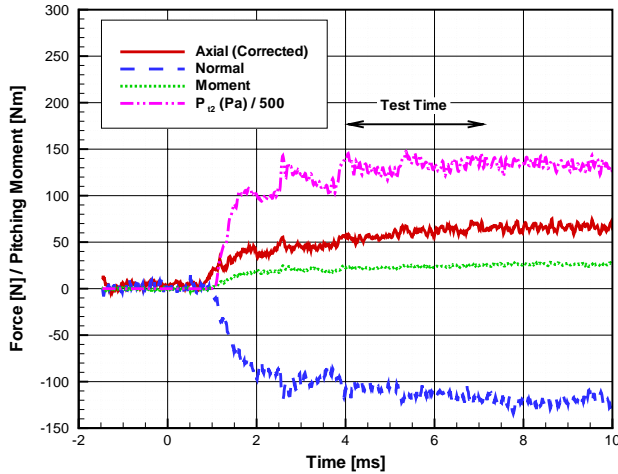


(a) Recovered time histories of force and pitching moment for run 687.

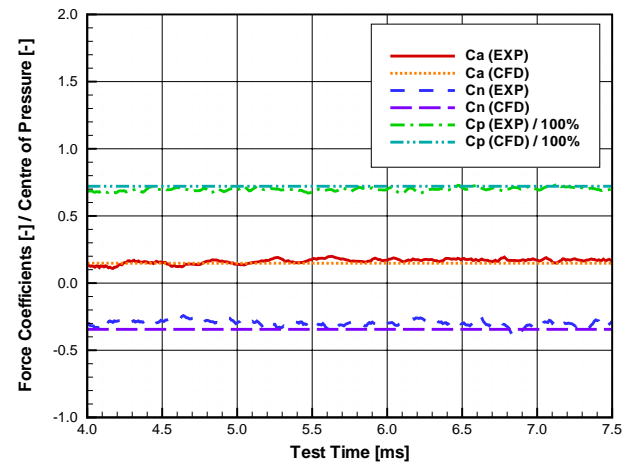


(b) Measured and theoretical force coefficients for run 687.

Figure 8. Condition XI blunt cone results at 0° angle of attack.



(a) Recovered time histories of force and pitching moment for run 685.



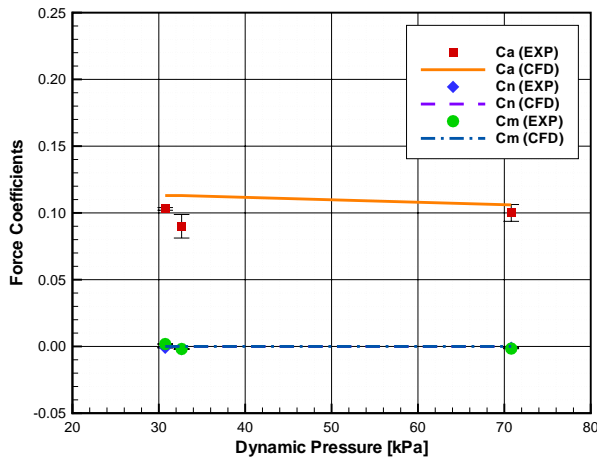
(b) Measured and theoretical force coefficients for run 684.

Figure 9. Condition XII blunt cone results at -10° angle of attack.

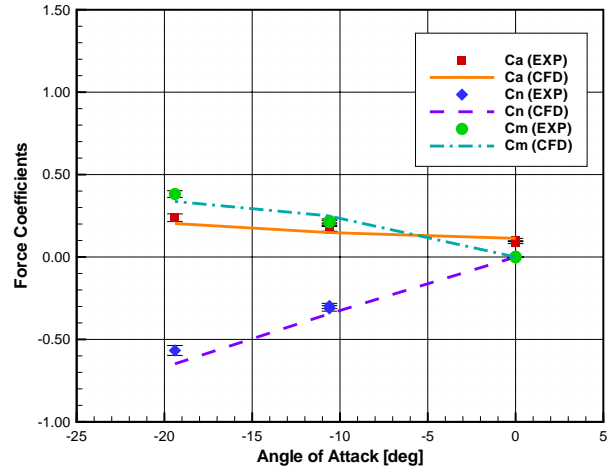
An example of the time recovered force coefficients for run 684 (also performed at -10°) is given in Fig. 9 (b). The corresponding theoretical magnitudes from CFD simulations are also shown. The recovered axial and normal coefficients agree to within 6 and 9% respectively of the theoretical values. The center of pressure is recovered to within 2% (as a percentage of chord).

The insensitivity of the drag coefficient with dynamic pressure at 0° angle of attack over HEG conditions XI and XII is illustrated in Fig. 10 (a). An average drag coefficient of 0.10 was obtained and this compares to a value of 0.11 from the CFD.

Fig. 10 (b) shows the recovered force coefficient magnitudes with a variation in angle of attack. It is noted that generally a linear decrease in normal force and a linear increase in the axial force is obtained with decreasing angles of attack. The pitching moment coefficient exhibits a non-linear trend but given the limited number of angles of attack tested, it is difficult to further define the trend.



(a) Measured and theoretical force coefficients versus dynamic pressure at 0° angle of attack.



(b) Measured and theoretical force coefficients versus angle of attack at 0° angle of attack.

Figure 10. Blunt cone force coefficients.

B. HB-2 Model

The HB-2 model was tested at condition III at 0° angle of attack. An example of the time history of the recovered force at condition III is shown in Fig. 11. Also shown is the measured Pitot pressure (normalized to unity) and then scaled with the CFD predicted drag force.

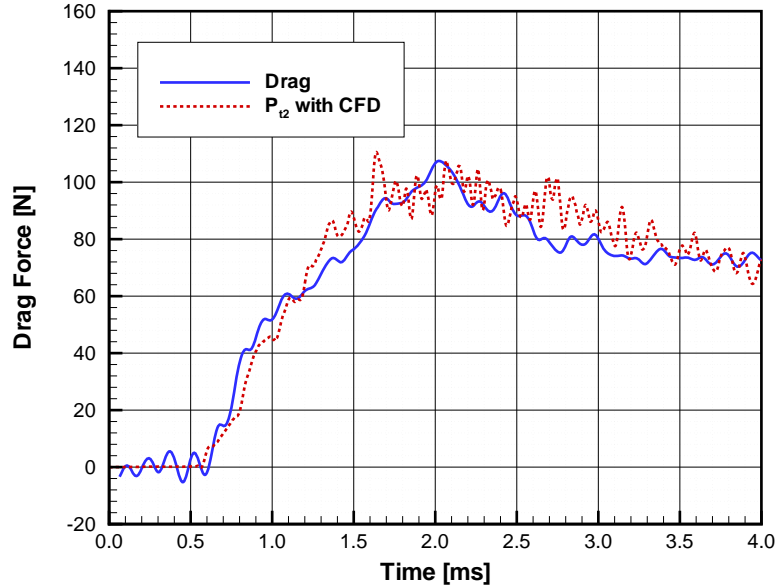


Figure 11. Measured drag force for the HB-2 model at condition III with the corresponding Pitot pressure scaled by the CFD predicted force.

Additional runs at condition III at 0° angle of attack are summarized in Fig. 12. Shown in this figure is a comparison of the axial force coefficient with the viscous interaction parameter ($\chi = Ma/\sqrt{Re_d}$). In order to obtain the ρu^2 quantity to determine the axial force coefficient, the recovered force was normalized with the quantity $P_{t2}/0.96$ since,

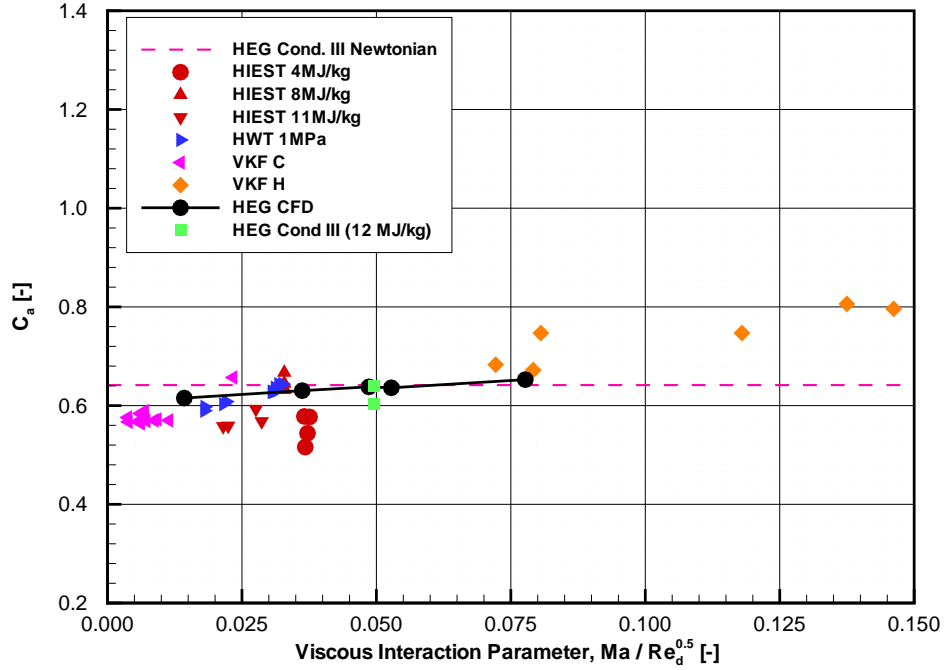


Figure 12. Axial force coefficient versus viscous interaction parameter.

$$P_{t2} = 0.96\rho u^2, \quad (6)$$

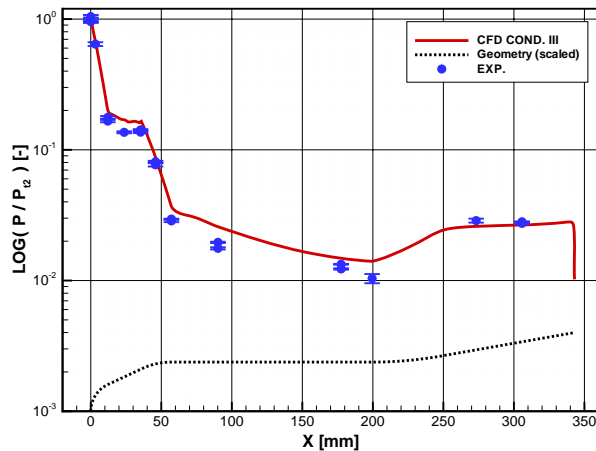
at condition III. Additional data from Hiest, HWT and VKF are shown. CFD and Newtonian predictions for the HEG HB-2 model are also shown. Good comparison between the measured forces, the CFD and results from the other wind tunnels is obtained.

The corresponding pressure and heat flux distributions are compared to the CFD simulations in Fig. 13. The measured pressures were normalized by the Pitot pressure while the heat flux was normalized by the stagnation heat flux measured on the HEG permanent probe. It is noted that in general, the pressure is slightly over-predicted. This is hypothesized to be due to the conical nature of the flow for condition III.

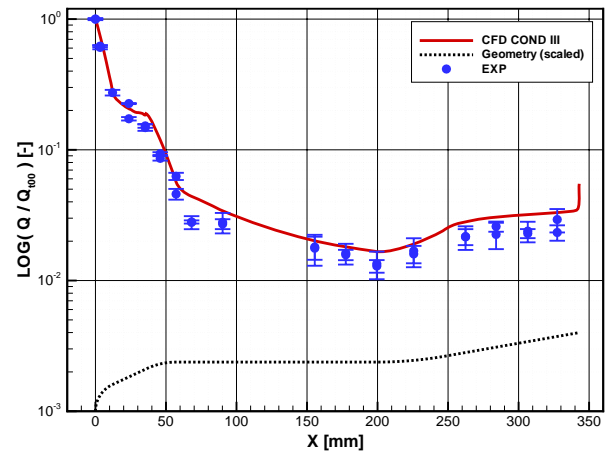
VII. Conclusion

The three component force balance presented has been designed for short duration force measurements. Experiments performed on a blunt cone in a shock tunnel showed adequate response time of the force balance and recovery of the force components to within suitable uncertainties. At -10° , the axial and normal coefficients were within 6% and 9% respectively of CFD predictions, while the center of pressure (based on chord length) was within 2%. More accurate knowledge of the free-stream conditions and additional pressure and heat transfer measurements on the cone would aid in identifying these differences and provide greater certainty in the CFD predictions. The uncertainties in the force measurements are estimated at around $\pm 5\%$ for the axial component and $\pm 4\%$ for the normal and pitching moment components at condition XI. At condition XII, the axial force uncertainty increases to around $\pm 9\%$ due to the additional uncertainty regarding the pressure increase in the shielding cavity. This could be reduced by using a more sensitive pressure transducer.

Tests were also conducted on a standard force reference model, HB-2, at condition III at 0° angle of attack. Measured heat flux and pressure distributions along the HB-2 model compared well with non-equilibrium CFD predictions. It is hypothesized that better agreement of the measured pressures could be obtained if a far-field boundary condition that accounted for the conical nature of the flow was used. Future tests at other HEG operating conditions (both low and high enthalpies) are planned.



(c) Condition III pressure distribution



(d) Condition III heat flux distribution

Figure 13. Pressure and heat flux distributions compared to CFD for condition III on the HB-2 model.

Acknowledgments

The authors would like to thank Ingo Schwendtke for operating the HEG facility. Sebastian Karl is acknowledged for CFD nozzle simulations and Jan Martinez Schramm is also acknowledged for his assistance during the experiments.

References

- ¹Paull, A., Alesi, H., and Anderson, S., "The HyShot flight program and how it was developed," *11th AIAA / AAAF Space Planes and Hypersonic Systems and Technologies Conference*, Orleans, France, September 2002.
- ²Weihs, H., Longo, J. M. A., and Gülhan, A., "The Sharp Edge Flight Experiment SHEFEX," *4th European Workshop on Hot Structures and Thermal Protection System for Space Vehicles*, Palermo, Italy, November 2002.
- ³Carbonaro, M., "Aerodynamic force measurements in the VKI Long Shot hypersonic facility," *New Trends in Instrumentation for Hypersonic Research*, ONERA Le Fauga - Mauczac, France, April 27-May 1 1992, pp. 317–325.
- ⁴Störkmann, V., Olivier, H., and Grönig, H., "Force measurements in hypersonic impulse facilities," *AIAA Journal*, Vol. 36, No. 3, 1998, pp. 342–348.
- ⁵Naumann, K. W., Ende, H., Mathieu, G., and George, A., "Millisecond aerodynamic force measurement with side jet model in the ISL shock tunnel," *AIAA Journal*, Vol. 31, No. 6, 1993, pp. 1068–1074.
- ⁶Sanderson, S. R. and Simmons, J. M., "Drag balance for hypervelocity impulse facilities," *AIAA Journal*, Vol. 29, No. 12, 1991, pp. 2185–2191.
- ⁷Mee, D. J., Daniel, W. J. T., and Simmons, J. M., "Three-component force balance for flows of millisecond duration," *AIAA Journal*, Vol. 34, No. 3, 1996, pp. 590–595.
- ⁸Paull, A., Stalker, R. J., and Mee, D. J., "Scramjet thrust measurement in a shock tunnel," *The Aeronautical Journal*, Vol. 99, No. 984, April 1995, pp. 161–163.
- ⁹Stalker, R. J. and Paull, A., "Experiments on Cruise Propulsion with a Hydrogen Scramjet," *The Aeronautical Journal*, Vol. 102, No. 1011, January 1998, pp. 37–43.
- ¹⁰Prost, R. and Goutte, R., "Discrete constrained iterative deconvolution algorithms with optimized rate convergence," *Signal Processing*, Vol. 7, No. 3, 1984, pp. 209–230.
- ¹¹Gray, J. D., "Summary report on aerodynamic characteristics of standard models HB-1 and HB-2," Aedc-tdr-64-137, July 1964.
- ¹²Kuchi-ishi, S., Watanabe, S., Nagai, S., Tsuda, S., Koyama, T., Hirabayashi, N., Sekine, H., and Hozumi, K., "Comparative force/heat flux measurements between JAXA hypersonic test facilities using standard model HB-2 (Part 1)," Jaxa research and development report, jaxa-rr-04-035e, March 2005.
- ¹³Hannemann, K., "High Enthalpy Flows in the HEG Shock Tunnel: Experiment and Numerical Rebuilding," *AIAA 2003-0978, 41st AIAA Aerospace Sciences Meeting and Exhibit*, Reno, 6-9 January 2003.
- ¹⁴McIntosh, M. K., "Computer program for the numerical calculations of frozen and equilibrium conditions in shock tunnels," Software CR-181721, The Australian National University, 1968.
- ¹⁵Hannemann, K., Schnieder, M., Reimann, B., and Martinez Schramm, J., "The influence and delay of driver gas contamination in HEG," *21st AIAA Aerodynamic Measurement Technology and Ground Testing Conference*, Denver, CO, AIAA Paper 2000-2593, 19-22 June 2000.

¹⁶Gerhold, T., Friedrich, O., Evans, J., and Galle, M., "Calculation of Complex Three-Dimensional Configurations Employing the DLR-TAU-Code," AIAA-paper 97-0167, 1997.

¹⁷Gupta, R., Yoss, J., Thompson, R., and Lee, K., "A review of reaction rates and thermodynamic transport properties for an 11-species air model for chemical and thermal nonequilibrium calculations to 30 000K," Tech. Rep. NASA-RP-1232, 1990.